

# Design and identification of parameters of tuned mass damper with inerter which enables changes of inertance

M. Lazarek, P. Brzeski\*, P. Perlikowski\*

*Division of Dynamics, Lodz University of Technology, Stefanowskiego 1/15, 90-924 Lodz, Poland*

---

## Abstract

In this paper we show the design of a novel tuned mass damper with inerter that enables changes of inertance. We present the details of the experimental rig that is used to test the prototype device and provide technical documentation of its crucial elements. The mathematical model of the system is derived based on the Lagrange equations of the second type. We identify the parameters of the system: masses, stiffnesses of springs and damping coefficients. We pay special attention to identification of energy dissipation model composed of viscous damping and Coulomb damping. We use two step procedure to find the proper values of damping coefficients with high precision. To validate the model we compare the numerical and experimental time traces. Good matching of the results prove well-posedness of the model and confirm the obtained parameter values.

*Keywords:* Inerter, tuned mass damper, prototype, experimental investigation, energy dissipation

---

## 1. Introduction

The mitigation of structural vibrations is now a strongly developed area of engineering. The classical tuned mass dampers (TMD) are well known and widely used. However, their efficiency can be increased by modifications of the design. One of the promising ideas is to add an inerter to the TMD. Inerter has been proposed by Malcolm Smith [27] in 2002. It is a two terminal device in which force is proportional to the relative acceleration of its ends. There are two most common realizations of the inerter. The first one is a mechanical device where the linear motion is changed into rotations of the flywheel via mechanical gear and the energy is transferred into rotations of the flywheel [12, 28]. In the second realization the mechanical gear is substituted with a hydraulic device [30]. There are multiple significant applications of inerters, which are used to absorb impact forces [10, 25] or protect buildings from earthquakes [31, 9]. In [8] authors study the influence of the inerter on the natural frequency of system's vibrations. The influence of different types of inerter' nonlinearities (viscous damping, dry friction and play in the inerter gears) has been studied in our previous paper [5]. We show that in many cases, the simplified model of the device enables to obtain results with satisfactory precision.

When designing a mechanical or a structural system one can predict the approximate values of system parameters. The mass and the stiffness are relatively easy to validate. The challenging task is usually to find the proper model of the energy dissipation [20, 22, 1, 17]. We assume that in the considered system the dissipation occurs via viscous damping and dry friction. Feeny and Liang [11, 13] presented the method to extract the viscous damping coefficient and dry friction force from free oscillations. They show that for linear system one can analytically calculate the fraction of viscous damping and dry friction force in overall energy dissipation. In [14] the estimation of both parameters has been performed using the response of the forced system using the energy balance method. Both methods are efficient for analysis of linear systems which

---

\*Corresponding author

*Email address:* piotr.brzeski@p.lodz.pl (P. Brzeski)

oscillate harmonically. However, most experiments reveal some divergence from harmonic motion which is caused by non-harmonic excitation, non-linearity of springs and dampers, bearings jamming and many more. Hence, based on the analytical method we can only estimate parameter values to use them as the first guess for more sophisticated identification methods. There are many methods for system identification [15, 16, 19], but the gray box [21] and the black box [26, 24] modelling are most popular. If one knows the mathematical model of analyzed system the gray box model enables to estimate the values of parameters. However, if we do not have the equations of motion we have to use the black box model to find the proper formulas and parameter values.

In [3] we propose the concept of the new TMD design with inerter that enables changes of inertance and in [4] we give the experimental proof of concept. The main advantage of the proposed device is the possibility to tune the natural frequency of the TMD to the current frequency of the excitation. This feature is obtained by implementing the continuously variable transmission (CVT) to the inerter. CVTs become widely use as an alternative for gear transmissions in vehicles powertrains increasing performance and power economy [29]. Hence its design and efficiency has been studied [7]. Further analysis concerns heat transfer [32] and extensions including neutral gear [2]. Ability to stepless change of ratio realized into a small space is useful also for bikes [18, 23]. In [3, 4] we prove that the proposed TMD design enables to reduce the amplitude the damped structure vibrations to very low values (significantly smaller than in the system without the TMD).

The proposed TMD design consists of some specific mechanisms that are crucial for its performance and reliability. For example the inerter with the CVT has been designed and built specifically for the purpose. In this paper we describe the details of the design of the prototype device and the experimental rig. We indicate the most critical elements of the TMD and present their construction. Apart from that, we indicate the sources of nonlinearities in the model and investigate their influence on the dynamical response of the system. Then, we consider different sources of energy dissipation in the system. We investigate them separately and propose overall simplified energy dissipation model that can facilitate the dynamical analysis. We perform a series of dedicated tests to estimate parameter values and validate the model of the system experimentally. We consider both free vibrations and excited motion to prove the robustness of the energy dissipation model. It is especially important because, as indicated in [3, 4], damping in the TMD strongly influences its efficiency and the range of effectiveness.

The paper is organized as follows, in Section 2 we describe the design of the prototype and the experimental rig. The model is presented in Section 3. In Section 4 we show the details of measurement setup and the strategy to obtain system's parameters. We also compare the numerical and experimental time traces. The model of the excitation mechanism and comparison of the experimental and numerical time traces of the forced system are shown in Section 5. Finally, we summarize and conclude our work in Section 6.

## 2. Description of the rig design

The laboratory rig consists of two one degree-of-freedom oscillators. The first (main) oscillator has dominant mass and is forced externally. Our aim is to mitigate its vibrations by the addition of the specific TMD. Particularly, the novel TMD design that enables stepless changes of inertance to tune its natural frequency to the current frequency of excitation. To ensure proper operation of the rig we make several design assumptions, requiring:

- ability to test different TMD/CVT embodiments,
- ability to test performance of the novel type of TMD in a wide range of excitation frequencies,
- ability to control the amplitude and the frequency of kinematic excitation,
- ability to change parameter values of the main mass assembly,
- easy modifications of the rig structure,
- low manufacturing cost,

- minimum energy dissipation in the guiding of the TMD.
- minimum internal damping of the CVT.

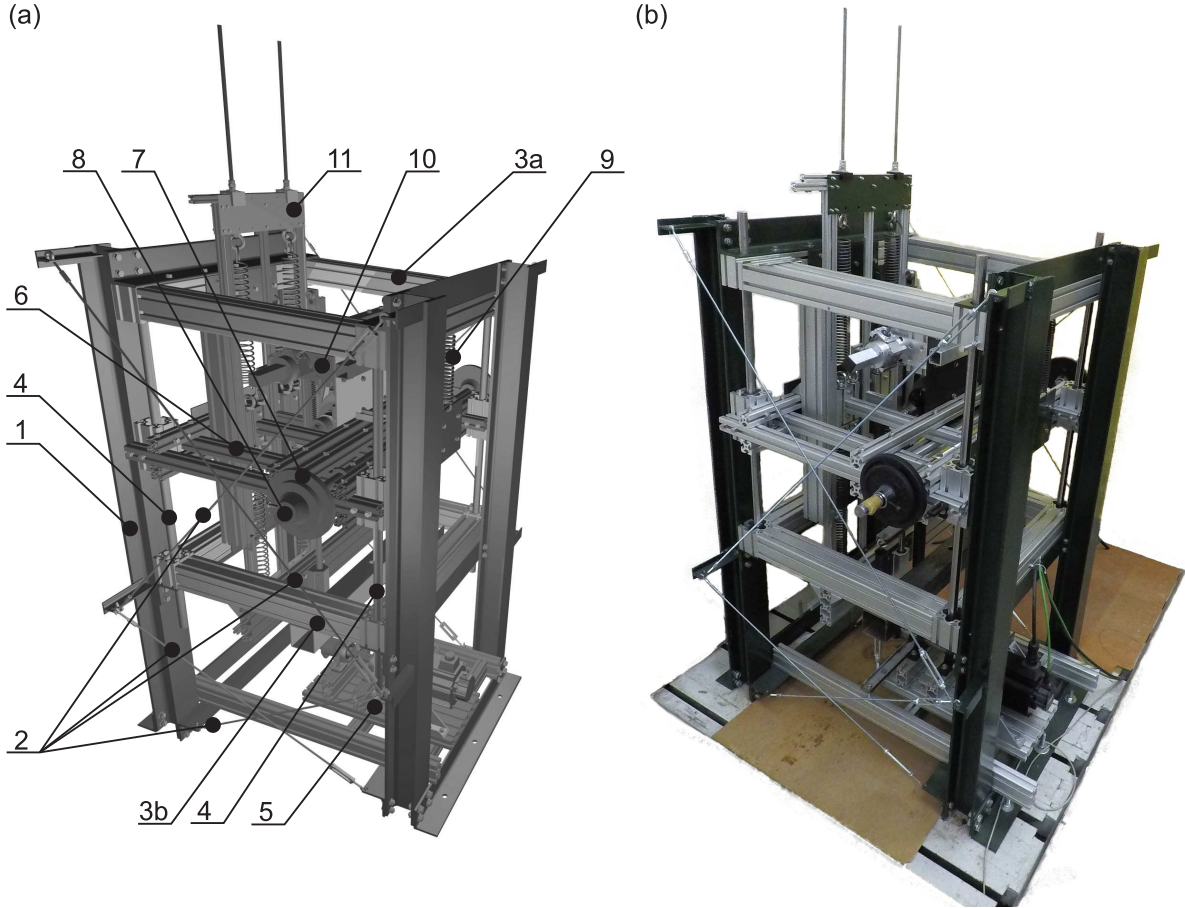


Figure 1: Design of the laboratory rig (a) and its realization (b). Parts presented in the figure: 1 - Outer steel structure, 2 - Struts, 3a and 3b - Main inner structure, 4 - Guide shaft, 5 - Kinematic excitation assembly, 6 - Main oscillator structure, 7 - Mass elements, 8 - Barbell, 9 - Main springs (1 visible out of 6), 10 - CVT assembly, 11 - Moving part of the TMD. Additional exploded view of the rig is presented in Appendix.

Moreover, to ensure good damping efficiency and preserve the advantages of the considered TMD design we have to overcome a number of design and manufacturing challenges. The two most challenging issues are to design the CVT and guiding for the TMD with low motion resistances. Both issues are crucial, because in our previous paper [3] we have shown that the damping efficiency drops with the increase of internal damping of the TMD. When designing the CVT, we have to find the optimal tradeoff between the maximum transmitted torque and motion resistance. It is especially important because all known CVT designs include prestressed elastic elements to prevent slip and enable transmission of torque. Unfortunately, these elements cause energy dissipation even when the gear load is small. Similarly, for guiding of the TMD our aim is to select the design that has the least motion resistances and provides the required load capacity.

The considered experimental rig is the updated version of the setup considered in [4]. Comparing current design of the rig with earlier version we modified the TMD guiding, CVT, TMD frame and some minor parts of the main oscillator. The aim of redesigning was to improve the reliability and versatility of

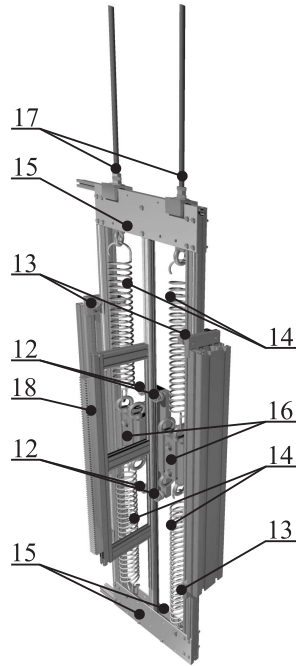


Figure 2: Isometric view of the TMD. Parts presented in the figure: 12 - Main rollers, 13 - Side rollers, 14 - TMD springs, 15 - Spring plates, 16 - Spacing spring blocks, 17 - Tension rods, 18 - Gear rack.

the rig. Considering different possible realizations of design guidelines we created the rig presented in Fig.1. Additionally we create exploded view (see Appendix) of the rig where main subassemblies are presented separately. Note that outer steel structure is excluded from the view. The system shown in Fig.1 consists of one degree of freedom kinematically forced oscillator and the prototype TMD. The frames of the main mass and the TMD are made from aluminum and steel profiles. The outer steel structure No. 1 has a square base of  $\square 0.7$  [m] and is 1.6 [m] of height. The arrangement of struts (parts No. 2) is introduced to increase the rigidity. The outer steel frame supports the main inner structure (parts No. 3 (a,b)) in which four main guide shafts (parts No. 4) are positioned. Additionally, the outer steel structure also holds the kinematic excitation assembly (part No. 5). The main mass oscillator assembly is suspended with six springs (part No. 9 - only one out of six is visible) whose second ends are fixed to the main inner structure. The main oscillator is a frame made from aluminum profiles. Four vertically mounted profiles on its corners are used as a linear bearing housings. The barbell (part No. 8) enables to add mass elements (parts No. 7) to adjust the overall mass of the main oscillator. The main oscillator frame supports the CVT assembly (part No. 10) and the flywheel of the TMD at its driven shaft.

The moving part of the TMD (part No. 11) with mass  $m$  is presented in Fig. 2. The structure is guided through the system of the main rollers and the side rollers (parts No. 12 and No. 13). It performs vertical movement with relation to the main mass assembly. The TMD is suspended using four springs (parts No. 14) which connect spring plates (parts No. 15) with the spacing blocks (part No. 16) mounted to the main mass structure. The springs have preload obtained by tension rods (parts No. 17) and enable to shift the equilibrium position to the middle of TMD oscillating range. The design ensures sufficient rigidity and good strength-to-weight ratio. Vertical movement of the TMD is converted to the rotational motion by the gear rack (part No. 18) placed with an offset from the plane of motion which ensures space for the CVT. The

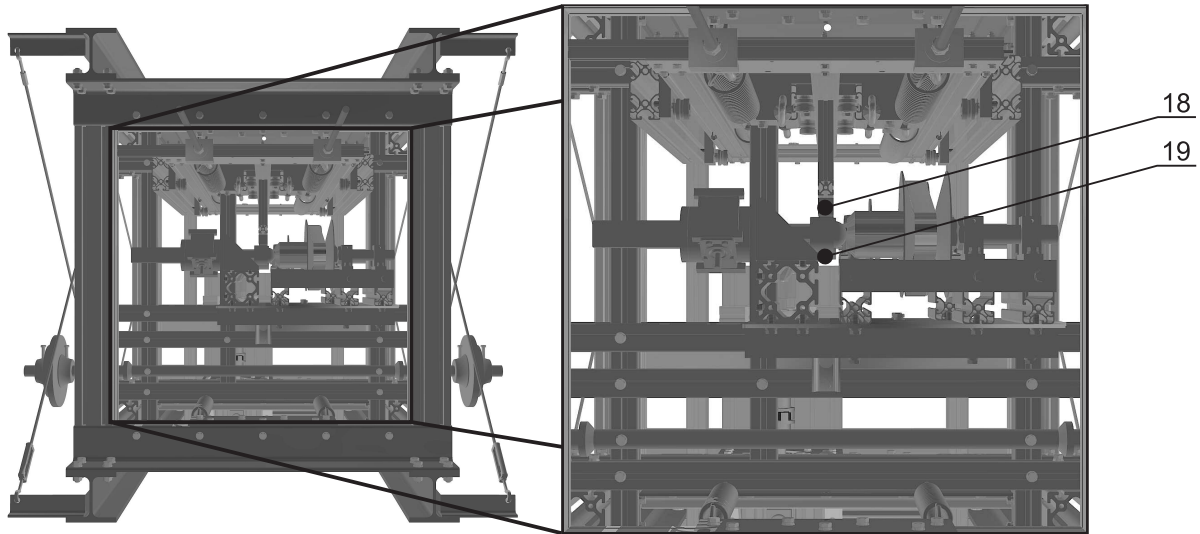


Figure 3: Top view of the laboratory rig. Parts presented in the figure: 18 - Gear rack, 19 - Gear.

gear rack (part No. 18) is cooperates with a gear (part No. 19) on the drive shaft of the CVT as presented in Fig. 3. The belt-driven CVT presented in Fig. 4 uses modified parts from LinHai ATVs. It consists of the drive shaft (part No. 20) supported in ball bearing units (parts No. 21) which are connected to the base made from the aluminum profiles (parts No. 22) and then to the CVT mounting plate (part No. 23). On the second end of the CVT, we mount the stationary driven shaft (part No. 24) held by shaft supports (parts No. 25) which are similarly placed on the aluminum profiles connected to the CVT mounting plate. Original centrifugal mechanism of the CVT used to change the gear ratio is replaced by two modified rear clutch pulley assemblies. The CVT drive shaft is directly connected to the first modified clutch pulley assembly. It consists of original pulley plates (parts No. 26) and components that allow to correcting belt (part No. 27) compression and torque transmission, namely the spring (part No. 28) and the spring retainer plate (part No. 29). On the second end of the CVT transmitted torque drives a pair of original pulley plates which spacing is controlled. The control mechanism enables to change of the CVT ratio using screw mechanism (part No. 30). The ball transfer unit (part No. 31) is mounted at the end of the screw to provide the transfer of the control force to the brass sleeve (part No. 32) which is installed on the outside pulley plate. The transfer unit also allows to compensate the differences in rotational speeds between the driven shaft and the control screw mechanism. To reduce those differences the ball transfer unit is positioned by its base (part No. 33) to have a contact point in the center of brass sleeve.

Kinematic forcing presented in Fig. 5 is realized with the Panasonic MINAS A5 (part No. 34) servomotor mounted on a plate (part No. 35). It is supported with an angle brackets (parts No. 36) and screwed to the excitation base (part No. 37). The servo output shaft is connected to the main excitation shaft (part No. 39) by the claw clutch (part No. 38). The main excitation shaft is supported with ball bearing units (parts No. 40) which are placed on the aluminum profiles (parts No. 41) mounted on the excitation base. The main excitation shaft ends with a sleeve (part No. 42) and a crank regulation disk (part No. 43). The crank is regulated by changing the position of a short shaft (part No. 44) with respect to the main shaft axis. The short shaft is a revolute joint for a connection rod (part No. 45) ended with a piston (part No. 46). The piston head is used to mount a vertical shaft (part No. 47) exerting excitation on the main mass by the spring with the same stiffness as the springs supporting the main structure (not shown in the described figure). The vertical shaft is guided through a linear bearing unit (part No. 48) connected to the main inner structure by a mounting plate (part No. 49) connected to the crank mechanism. The servomotor posses 1.5 [kW] of the nominal power and 7.16 [Nm] of the nominal torque. The servomotor is controlled

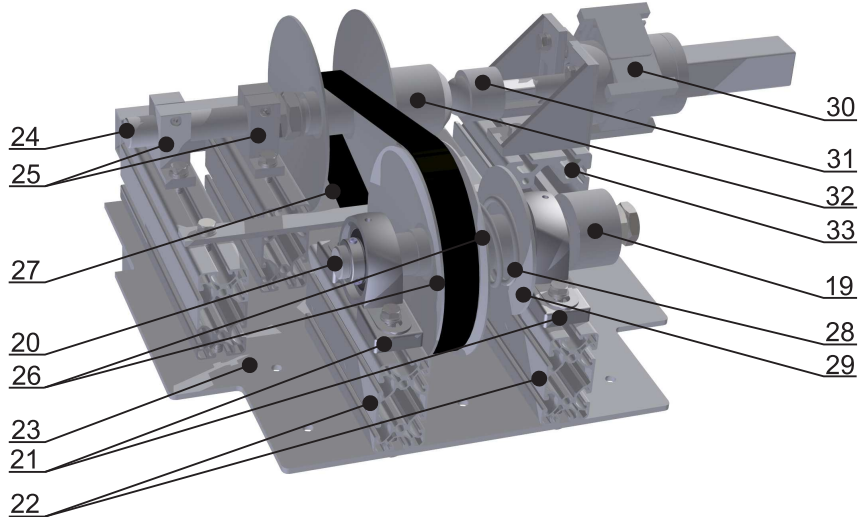


Figure 4: Isometric view of the CVT. Parts presented in the figure: 19 - Gear, 20 - Drive shaft, 21 - Bearing units, 22 - Aluminum profiles, 23- CVT mounting plate, 24 - Stationary driven shaft, 25 - Shaft supports, 26 - Pulley plates, 27 - Belt, 28 - Spring, 29 - Spring retainer plate, 30 - Screw mechanism, 31- Ball transfer unit, 32 - Brass sleeve, 33 - Control system base.

by Panasonic FP-X C30 PLC controller. Such configuration enables to change servo rotational speed with the accuracy of 1.0 [rpm] which corresponds to 0.105 [rad/s] and 0.0167 [Hz] (assuming the accuracy of three significant figures).

At present, the rig has been designed to proof the idea of the frequency controlled tune mass damper. It allows to test different configurations of CVTs and sizes of flywheels affecting the final performance of the device. However, the rig also enables to test differeny types of TMDs and ensures easy control of the parameter values that are described in the next Section.

### 3. Mathematical model of the rig

The considered mathematical model of the experimental rig is conceptually the same as the one considered in our previous paper [4]. Now we consider the updated model with more sophisticated energy dissipation model. In Fig. 6 we show two schematic diagrams that refer to the analysed model. In panel (a) we present more detailed model while in panel (b) simplified model with reduced number of parameters. Despite the level of details the model has two degrees of freedom and consists of two coupled oscillators that can move in the vertical direction. The first oscillator refers to the model of the main oscillator. The second oscillator is connected to the first one and represents the TMD. Both oscillators are connected via linear spring, viscous damper, inerter and element that models dry friction.

The motion of the system is described by two generalized coordinates: the position of the main oscillator by coordinate  $x$ , while the displacement of the TMD by coordinate  $y$ . The main oscillator is characterized with the following parameters:  $M$  is its mass,  $K$  is the stiffness of the single spring that connects the main mass to the ground,  $C$  is the viscous damping coefficient of dash-pot that links mass  $M$  and the support and  $D$  is the amplitude of dry friction force. The system is forced kinematically via a spring of stiffness  $K$  with the displacement  $a(t)$ . The excitation mechanism is described in details in Section 5.

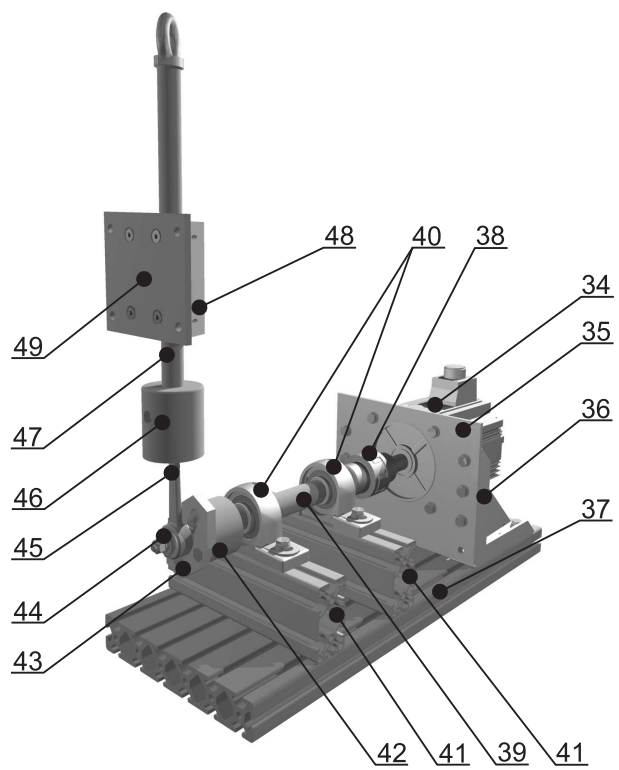


Figure 5: Isometric view of the excitation assembly. Parts presented in the figure: 34 - Servomotor, 35 - Servo plate, 36 - Angle brackets, 37 - Excitation base, 38 - Claw clutch, 39 - Main excitation shaft, 40 - Bearing units, 41 - Bearing units bases, 42 - Sleeve, 43 - Crank regulation disk, 44 - Short shaft, 45 - Connection rod, 46 - Piston, 47 - Vertical shaft, 48 - Bearing unit, 49 - Mounting plate.

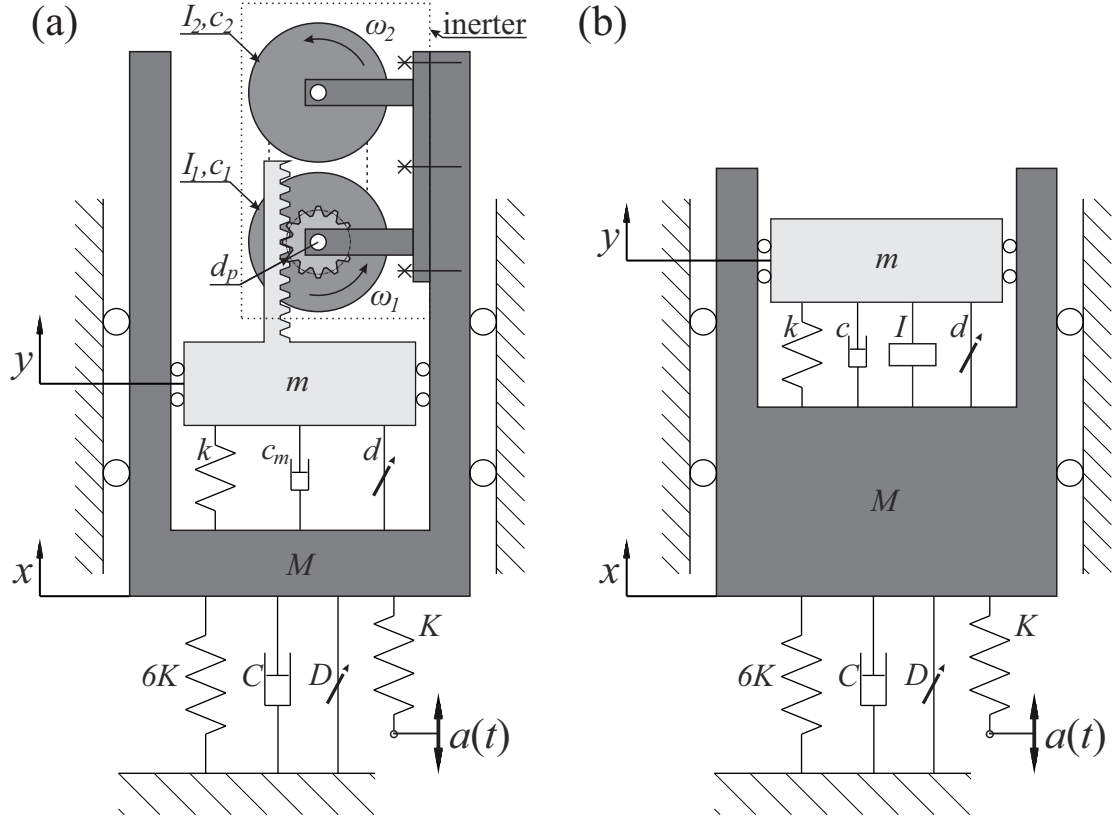


Figure 6: Physical model of the system and notation of parameters with different level of details.

Scheme presented in panel (a) contains comprehensive presentation of the TMD model. To characterize this system we use the following parameter values: the moving mass is given by  $m$ , the stiffness of the spring that connects it to the main oscillator is described with parameter  $k$ . The viscous damping coefficient of the dash-pot that connect mass  $m$  with  $M$  is given by  $c_m$  while  $d$  is the amplitude of dry friction force that is generated between the interacting parts. The pitch diameter of the pinion that cooperates with the moving rack is given by  $d_p$ ; the inertia of the drive shaft of the CVT is given by  $I_1$  and its rotational speed is described by  $\omega_1$ . For the driven shaft that is combined with the flywheel we use  $I_2$  and  $\omega_2$  respectively. We assume that the motion of each shaft of the CVT is damped with the torque proportional to its velocity. Damping coefficients are given by parameter  $c_1$  and  $c_2$  for the drive and driven shaft respectively. Parameter  $r$  is the current ratio of the CVT.

Before we derive the equations of motion of the system presented in Fig. 6(a) we introduce relations between the introduced parameters and coordinates. The rotational speeds of the CVT shafts can be calculated using the following formulas:

$$\omega_1 = 2 \frac{\dot{y} - \dot{x}}{d_p}, \quad (1)$$

$$\omega_2 = r \omega_1. \quad (2)$$

The total kinetic energy  $T$ , potential energy  $V$  and Rayleigh dissipation function  $D$  of the considered system are given by the following formulas:

$$T = \frac{1}{2} M \dot{x}^2 + \frac{1}{2} m \dot{y}^2 + \frac{1}{2} I_1 \dot{\omega}_1^2 + \frac{1}{2} I_2 \dot{\omega}_2^2, \quad (3)$$

$$V = \frac{1}{2}6Kx^2 + \frac{1}{2}K(x - a(t))^2 + \frac{1}{2}k(y - x)^2. \quad (4)$$

$$D = \frac{1}{2}C\dot{x}^2 + \frac{1}{2}c_m(\dot{y} - \dot{x})^2 + \frac{1}{2}c_1\omega_1^2 + \frac{1}{2}c_2\omega_2^2. \quad (5)$$

Apart from the above we use a continuous model of dry friction and assume that the force generated in the the dry friction elements is given as:

$$D\frac{2}{\pi} \arctan(10^5(\dot{x})), \quad (6)$$

$$d\frac{2}{\pi} \arctan(10^5(\dot{x} - \dot{y})). \quad (7)$$

Using the Lagrange equations of the second kind we reach two second order ordinary differential equations (ODEs) that describe the motion of the system presented in Fig. 6(a). After simplification, the equations of motion can be written as follows:

$$M\ddot{x} + 7Kx + C\dot{x} + \left(\frac{1}{d_p^2}I_1 + \frac{r^2}{d_p^2}I_2\right)(\ddot{x} - \ddot{y}) + k(x - y) + \left(c_m + \frac{1}{d_p^2}c_1 + \frac{r^2}{d_p^2}c_2\right)(\dot{x} - \dot{y}) + D\frac{2}{\pi} \arctan(10^5(\dot{x})) + d\frac{2}{\pi} \arctan(10^5(\dot{x} - \dot{y})) = Ka(t), \quad (8)$$

$$m\ddot{y} - \left(\frac{1}{d_p^2}I_1 + \frac{r}{d_p^2}I_2\right)(\ddot{x} - \ddot{y}) - k(x - y) - \left(c_m + \frac{1}{d_p^2}c_1 + \frac{r^2}{d_p^2}c_2\right)(\dot{x} - \dot{y}) - d\frac{2}{\pi} \arctan(10^5(\dot{x} - \dot{y})) = 0. \quad (9)$$

To reduce the number of parameters and to simplify our model we propose the system that is presented in Fig. 6(b). Now, we use the simplified model of the inerter that is described only with the inertance  $I$ . Apart from that, we use the single dash-pot with varying damping coefficient  $c(I) = c_{const} + c_I I$ . Thanks to these changes, we interchange 7 parameters  $I_1, I_2, c_m, c_1, c_2, d_p, r$  with only two parameters that are defined as follows:

$$I = \frac{4}{d_p^2}I_1 + \frac{4r^2}{d_p^2}I_2, \quad (10)$$

$$c(I) = c_m + \frac{4}{d_p^2}c_1 + \frac{4r^2}{d_p^2}c_2 = c_{const} + c_I I. \quad (11)$$

Assuming the accessible range of the CVT ratios we calculate the range in which we can smoothly change value of parameter  $I$ . Then, we calculate the values of two constants  $c_{const}$  and  $c_I$  that describe the viscous damping in the system. The behaviour of the simplified model (see Fig. 6(b)) is governed by the following equations of motion:

$$M\ddot{x} + 7Kx + C\dot{x} + I(\ddot{x} - \ddot{y}) + k(x - y) + c(I)(\dot{x} - \dot{y}) + D\frac{2}{\pi} \arctan(10^5(\dot{x})) + d\frac{2}{\pi} \arctan(10^5(\dot{x} - \dot{y})) = Ka(t), \quad (12)$$

$$m\ddot{y} - I(\ddot{x} - \ddot{y}) - k(x - y) - c(I)(\dot{x} - \dot{y}) - d\frac{2}{\pi} \arctan(10^5(\dot{x} - \dot{y})) = 0. \quad (13)$$

All the values of parameters involved in the numerical model have been derived in a series of dedicated experiments that are described in Section 4. For integration we use RK45 method implemented in Matlab with relative and absolute errors equal to 1e-3 and 1e-6 respectively (default values). It is a fifth order Runge-Kutta method with a variable time step. It is important to notice that the well-posedness of the model has been preliminary confirmed in our previous paper [4] where we also show the potential efficiency of the device. System presented in this paper is modified version of the rig based on our experience gained during the first series of experimental investigations.

#### 4. Measurement of system parameters

In this section we present a full data that is needed to obtain the reliable numerical model of our experimental rig. In [4] we considered earlier version of the rig. We modified the TMD guiding, CVT, TMD frame and some minor parts of the main oscillator. The aim of redesigning was to improve the reliability and versatility of the rig. After the improvement, we performed a detailed measurement of parameter values that are included in the mathematical model of the rig.

The parameters of the system can be divided into two groups. In the first group we have parameters that can be measured directly (masses, stiffnesses of springs, lengths and dimensions). While in the second group, we have the parameters involved in the energy dissipation model. It is well known that the identification of energy dissipation mechanisms and parameter identification is often a challenging task [20, 22, 1]. The values of damping coefficients and dry friction forces have to be estimated in a specific parameter identification procedure.

To obtain experimental data we use the following sensors and data acquisition system. To detect the position of the main mass we use a precise laser sensor Microepsilon optoNCDT1302 with 0.2 [m] range. Another laser sensor Keyence LK-G157/LK-G152 together with the dedicated controller LK-GD500 is used for detecting the crank position. To measure the velocities of the main mass and the TMD we use with two Polytec HSV 700 sensor heads with two Polytec HSV2002 controllers. All signals are acquired with the Bruel and Kjaer frame type 3660 with 3050 input module. Such configuration allows us to acquire six high-precision inputs with frequency up to 51.2 [kHz]. All the signals are collected using the Pulse LabShop software with no further filtering of the data.

##### 4.1. Masses, moments of inertia and stiffnesses

The masses of all components of the main oscillator and the TMD have been weighed before the system was assembled. We take initial values of springs' stiffnesses from catalogs. However, those values may not be precise enough. To validate them we perform a simple experiment. We detach the TMD from the main mass to obtain one degree of freedom (DoF) system. We measure its natural frequency  $\alpha_1$  and then we add additional mass  $m_1 = 20$  [kg]. Then, we once again measure the natural frequency  $\alpha_2$ . The dissipation of energy is small, hence with good precision we can assume that the natural frequency is a function of mass and stiffness. Then, we obtain two equations:  $M\alpha_1^2 = K$  and  $(M + m_1)\alpha_2^2 = K$  with two unknowns and we calculate the exact values of mass and stiffness of the main oscillator. The same procedure is performed for fixed main oscillator to estimate parameters of the TMD. In this case, we consider the TMD as a one DoF oscillator and add 2 [kg] for the second trial. By that, we reach the final values of parameters:  $M = 102.66$  [kg],  $K = 8181.0$  [N/m],  $m = 12.82$  [kg],  $k = 10985.1$  [N/m].

To model the inerter with the CVT we have to get the range of accessible values of  $I$  (Eq. 10). Parameter  $d_p = 60$  [mm] which is a pitch diameter of the pinion was taken from the catalogue. The moment of inertia of both shafts  $I_1 = 0.0036$  [kgm<sup>2</sup>] and  $I_2 = 0.0027$  [kgm<sup>2</sup>] were derived basing on detailed 3D CAD models. We measure the accessible range of gear ratios  $r \in (0.58, 1.76)$  of the CVT. Then, we are able to evaluate the following achievable range of inertance  $I \in (4.72, 12.9)$  [kg].

##### 4.2. Dissipation in the main oscillator guiding

The main mass is guided by the set of linear bearings that move along four main guide shafts. The housings for the linear bearings are mounted to the main oscillator assembly. To estimate the energy dissipation we detach the TMD and measure free vibrations of the main mass assembly. In the first approximation, we use the method of Linag and Feeny [11, 13] to estimate the partitions of viscous damping and dry friction force. The obtained values do not reflect experimental measurements sufficiently, so we decide to implement the additional identification method. We use the gray box model identification algorithm implemented in Matlab identification toolbox. The algorithm is based on the minimizing estimation prediction error [15]. Model of the main oscillator used in the identification procedure is based on Eq. (12) with  $y$  component and its derivatives assumed to be zero. Hence, we obtain one DoF system given by second order ODE:

$$M\ddot{x} + 7Kx + C\dot{x} + D\frac{2}{\pi} \arctan(10^5 \dot{x}) = 0. \quad (14)$$

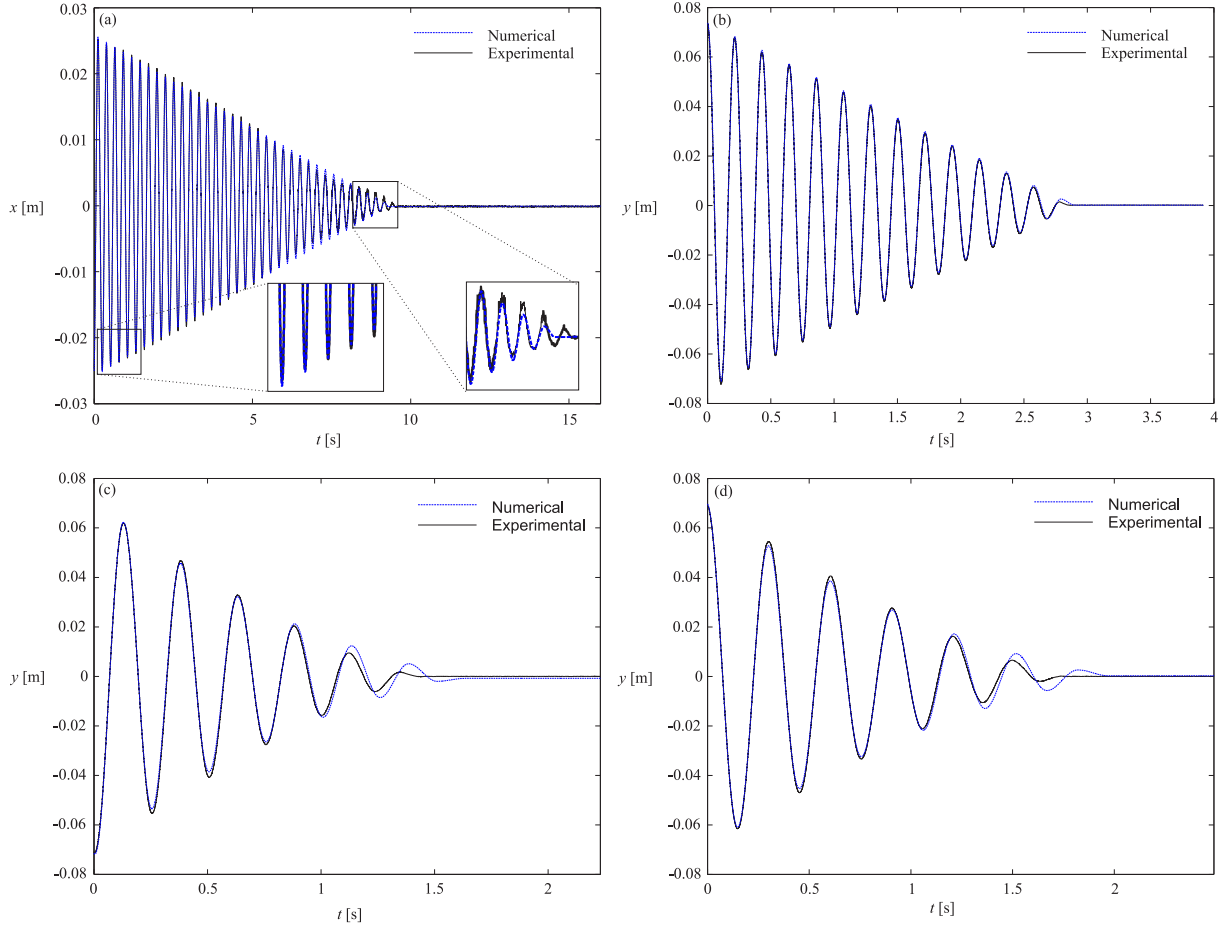


Figure 7: Comparison of the experimentally and numerically obtained time traces of free vibrations of the main oscillator (a), the TMD itself (b) and the TMD with the inerter and CVT (c,d).

The input parameters are  $K = 8181.0$  [N/m] and  $M = 102.66$  [kg]. The model quality evaluation is achieved by comparing simulated and measured displacements and calculating the normalized root mean squared error (NRMSE) using function implemented in Matlab. The value of fit is calculated as follows:  $NRMSE = 100 \left( 1 - \frac{\|r - \hat{r}\|}{\|r - \bar{r}\|} \right)$  [%], where  $r$  represents the experimental data,  $\hat{r}$  is an output from mathematical model and  $\bar{r}$  is a mean value of the experimental data. To have reliable results we perform identification procedure on 10 sample signals. The exemplary results are shown in Fig. 7(a) illustrating the accurate correspondence between data in the majority of time ( $NRMSE = 95.65$  [%]). One clearly visible inexactness appears during last part of motion. It is mainly caused by different friction decomposition. In the procedure we identify the viscous damping coefficient and the dry friction force which are  $C = 1.7688$  [Ns/m],  $D = 10.1270$  [N] (mean values form all samples) respectively.

#### 4.3. Dissipation in the TMD guiding

In the next step, we identify the dissipation in the TMD guiding created as the system of rollers - parts No. 12 and 13 presented in Fig. 2. Similarly to the previous Subsection we try to describe complex phenomena with overall dissipation model that includes viscous and Coulomb damping components and try to fit its parameter values to reproduce the observed behaviour with good precision. We consider TMD itself by disconnecting the CVT and in consequence the inerter. Then, in Eq. (13) we assume that  $x$  and its derivatives are equal to zero. Hence, the equation subjected to identification has one DoF and is as follows:

$$m\ddot{y} + ky + c_m\dot{y} + d\frac{2}{\pi} \arctan(10^5\dot{y}) = 0. \quad (15)$$

As aforementioned, the verified values of the mass and the spring stiffness are  $m = 12.82$  [kg] and  $k = 10985.1$  [N/m]. We perform parameters identification procedure similar to the one described in the previous subsection and we also test 10 samples. The exemplary comparison between experimental data and the result from direct numerical integration gives  $NRMSE = 96.99$  [%] fit and we present time traces in Fig. 7(b). Estimated parameter values are  $c_m = 0.0095$  [Ns/m],  $d = 15.0109$  [N] (mean values form all the considered samples). The last parts of numerical simulations differ from the measured data. However, differences are minor and we cannot expect that the same model of dissipation (with the same parameter values) will give an excellent fitting for both large, medium and small amplitudes of vibrations. Moreover, in our model we are interested in large and medium amplitudes because such range refers to the real working conditions.

#### 4.4. Dissipation in the CVT

The results presented in the previous subsection show that it is possible to model the energy dissipation in the linear guiding with overall dissipation model that includes viscous and Coulomb damping components. For that case the dry friction dominates while partition of the viscous damping is nearly zero. Now, we consider damping in the CVT of our design. However, when we add the CVT the viscous damping starts to play significant role in the overall dissipation model. Moreover, for varying ratios of the CVT the damping coefficient varies. That is why in our model viscous damping depends on the current ratio of the CVT (see Section 3 and Eq. (11)). Hence, the equation used in the identification procedure has the following form:

$$(m + I)\ddot{y} + ky + c(I)\dot{y} + d\frac{2}{\pi} \arctan(10^5\dot{y}) = 0, \quad (16)$$

where  $c(I) = c_{const} + c_I I$ . Parameter  $c_{const}$  is the constant component of the viscous damping coefficient in the CVT and inerter, while  $c_I$  is the inertance dependent part of the viscous damping coefficient. The damping coefficient  $c_m$  is included in  $c_{const}$ , hence it is not present in the equations. We fix the value of dry friction force by setting its value to  $d = 15.0109$  [N] (identified in the previous step) and we only identify the viscous dissipation parameters. We run the TMD with minimum and maximum ratios (10 times for each setting) and we find the corresponding viscous damping coefficients for each case. Exemplary results are shown in Fig. 7(c,d). Panel (c) corresponds to minimal  $I_{MIN} = 4.72$  [kg] and panel (d) to maximum  $I_{MAX} = 12.9$  [kg] inertance respectively. In panel (c) the correspondence between data is  $NRMSE = 92$  [%] and in panel (d) the fit is  $NRMSE = 93.3$  [%]. Decrease of data convergence is caused by smaller number of oscillations' periods in comparison to the main mass and the TMD itself. Basing on 10 runs we get the following results:  $c(I)_{MIN} = 28.7792$  [Ns/m] and  $c(I)_{MAX} = 32.7203$  [Ns/m] for total viscous damping coefficient for system with minimal and maximal inertance respectively. Hence, the constant and varying part of viscous damping coefficient can be calculated by solving the set of equations  $c(I)_i = c_{const} + c_I I_i$ , where  $i = 1, 2$ . The obtained constant viscous damping coefficient equals  $c_{const} = 26.5104$  [Ns/m] and varying part of viscous damping coefficient equals  $c_I = 0.4811$  [Ns/m]. To confirm the coefficients values we run multiple tests for CVT's ratios between the two extreme settings which proves good matching of the results.

## 5. Response of the system under external excitation

In the previous Section, we describe the procedure to measure and validate parameter values of the system without external forcing. In this section we analyse the mechanism of excitation implemented in our rig and show the response of the system under excitation. The forcing is realized by crank mechanism, hence it is not harmonic signal. We show its complete model and we analyse its possible simplifications by expansion in Taylor series. This is important if one want to study the dynamics of system using path-following or

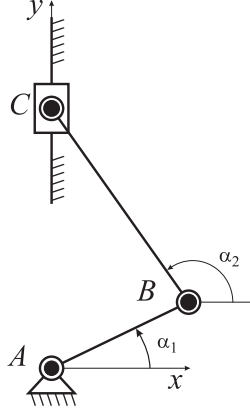


Figure 8: Scheme of the crank mechanism.

need information how the excitation diverges from the harmonic function. In Section 2 we provide the detailed description of the technical design of the mechanism. The forcing is kinematic and realized with the Panasonic MINAS A5 servomotor connected to the crank mechanism. Excitation is transmitted by the spring with the same stiffness as springs supporting the main structure (see part No. 9 in Fig. 1). Such configuration enables to change the frequency of excitation by varying the servo rotational speed with the accuracy of 1.0[rpm] which corresponds to 0.105[rad/s] and 0.0167[Hz] (assuming the accuracy of three significant figures).

The scheme of the considered crank mechanism is shown in Fig. 8 and consists of the crank and the connecting rod. In our case the crank has the length of 0.2955[m] and the connecting rod 0.12[m]. The spectrum of forcing signal, due to the structure of the crank, is composed of the main harmonic and the higher order harmonics. The mechanism can be described by the following vectors:  $\bar{l}_{AB}$ ,  $\bar{l}_{BC}$ ,  $\bar{l}_{AC}$  and corresponding angles:  $\bar{\alpha}_1$ ,  $\bar{\alpha}_2$ . The lengths  $l_{AB}$  and  $l_{BC}$  are given by the geometry of the crank mechanism, while the angle  $\alpha_1$  can be calculated based on the current angular velocity of the servomotor ( $\dot{\alpha}_1 = \omega_1$ ). The vector inequality  $\bar{l}_{AC} = \bar{l}_{AB} + \bar{l}_{BC}$  can be rewritten as a two scalar equations:

$$\begin{aligned} l_{AB} \cos \alpha_1 - l_{BC} \cos \alpha_2 &= 0, \\ l_{AB} \sin \alpha_1 - l_{BC} \sin \alpha_2 &= l_{AC}. \end{aligned}$$

Based on those formulas we can derive  $l_{AC}$  and  $\alpha_2$ . However, it is typical to represent the excitation function as the harmonic signal. Thus, we use the following relations:  $\sin \alpha_2 = \sqrt{1 - \cos^2 \alpha_2}$  and  $\cos \alpha_2 = -\eta \cos \alpha_1$ , where  $\eta = \frac{l_{AB}}{l_{BC}}$ . The  $\sin \alpha_2$  function can be approximated using a Taylor expansion:

$$\sin \alpha_2 = \sqrt{1 - \eta^2 \cos^2 \alpha_1} \approx 1 - \frac{1}{2} \eta^2 \cos^2 \alpha_1 - \frac{1}{8} \eta^4 \cos^4 \alpha_1 + \mathcal{O}(\eta^6 \cos^6 \alpha_1).$$

The powers of cosine functions can be represented as a series of the higher order harmonics as:  $\cos^2 \alpha_1 = \frac{1}{2}(1 + \cos(2\alpha_1))$  and  $\cos^4 \alpha_1 = \frac{1}{8}(3 + 4\cos(2\alpha_1) + \cos(4\alpha_1))$ . Hence, the final formula for the actual length  $l_{AC}$  is given by:

$$l_{AC} = l_{AB} \sin \alpha_1 + l_{BC} \left( 1 - \frac{1}{4} \eta^2 (1 + \cos(2\alpha_1)) - \frac{1}{64} \eta^4 (3 + 4\cos(2\alpha_1) + \cos(4\alpha_1)) \right).$$

Based on this formula the excitation amplitude  $a(t)$  presented in Fig. 6 is given as follows:  $a(t) = l_{AC} - l_{BC}$  and it varies periodically in the range  $(0, 2\pi)$ . In Fig. 9(a) we show the plot of  $l_{AC}$  without expansion and with expansion of the first, the second and the fourth order of  $\sin \alpha_2$  function in Taylor series (the third order expansion is the same as the second order due to the lack of odd coefficients in the expansion). In the first order expansion  $\sin \alpha_2 = 1$  so  $l_{AC}$  is the harmonic function. Nevertheless, the

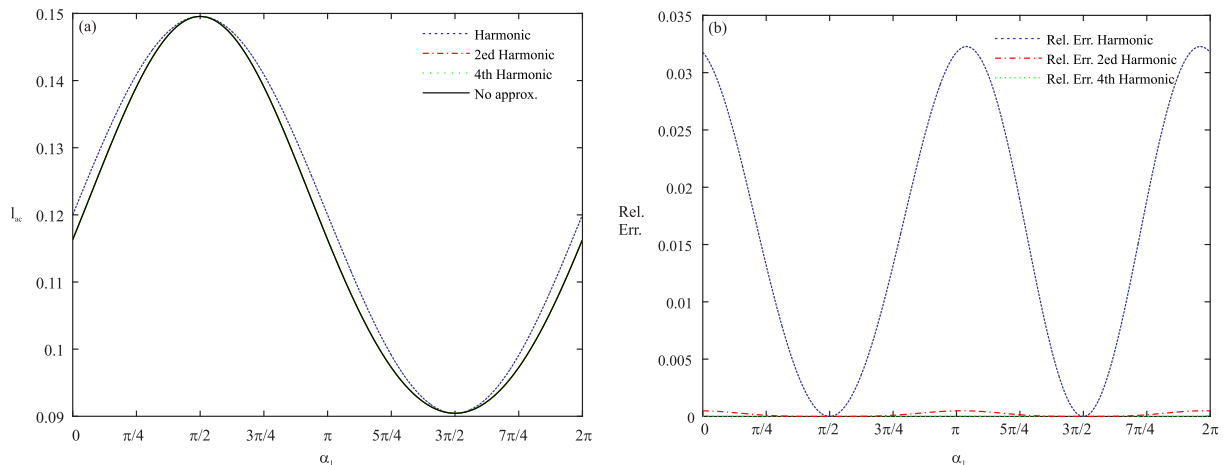


Figure 9: Distance  $l_{AC}$  in the considered crank mechanism without the expansion and for the first, the second and the fourth order of the expansion of  $\sin \alpha_2$  in Taylor series (panel (a)) and the relative error of the first, the second and the fourth order expansion in Taylor series with respect to the exact function.

higher order expansions give much better matching with the original function. The relative error of the first, the second and the fourth order with respect to the length  $l_{AC}$  calculated without expansion is shown in Fig. 9(b). The first order expansion has maximum relative error below 0.032 while for the higher order expansions in Taylor series the maximum relative error is  $4.9 \times 10^{-4}$  and  $1.5 \times 10^{-5}$ .

Now, we have all the necessary data to perform the comparison of experimental and numerical time traces of the forced system. We show the exemplary results for the fixed angular velocity of the servomotor  $s = 250$  [rpm] and two values of inertia  $I_1 = 6.36$  [kg] and  $I_2 = 12.9$  [kg]. We show them in Fig. 10. The matching of results is very good, so we claim that all parameters are identified correctly.

## 6. Conclusions

In this paper we show the comprehensive presentation of the specific TMD design. Its main feature is the possibility of stepless changes of inertia. The presented TMD is based on the idea proposed in our previous papers [3, 4] and its novelty is confirmed with the patent [6]. To prove the concept we design and build the rig with the prototype device. The presented version of the rig is in our opinion optimal and fulfil several crucial design's criteria.

We derive the mathematical model and identify the values of system parameters (masses, springs' stiffnesses and damping coefficients). Masses and stiffnesses of the main body and the TMD have been measured separately in a series of dedicated experiments.

In the next step we focus on the model of the the energy dissipation that is crucial for the efficiency and reliability of the TMD. In the considered experimental rig there are numerous sources of energy dissipation, however in our model we assume that it occurs via viscous damping and dry friction (Coulomb model). To find the partitions of the viscous damping and dry friction in overall dissipation in the first approximation we base on the Feeny and Liang method. Then, in the second step we tune the parameter values using the gray box model identification method. To illustrate the obtained results we compare the experimental and numerical time traces. In all cases we obtain very good matching. Hence, we claim that the proposed energy dissipation model is robust and the identification procedure was performed correctly and gave satisfactory results. As the last step, we describe the periodic excitation mechanism.

The rig incorporates different types of linear guiding, namely linear bearings and rollers, which have different energy dissipation mechanisms. In rollers the identified damping is similar in nature to Coulomb friction, while in linear bearing there is also significant viscous component. This difference is important and should be considered when designing mechanisms including linear guiding. In the considered CVT the

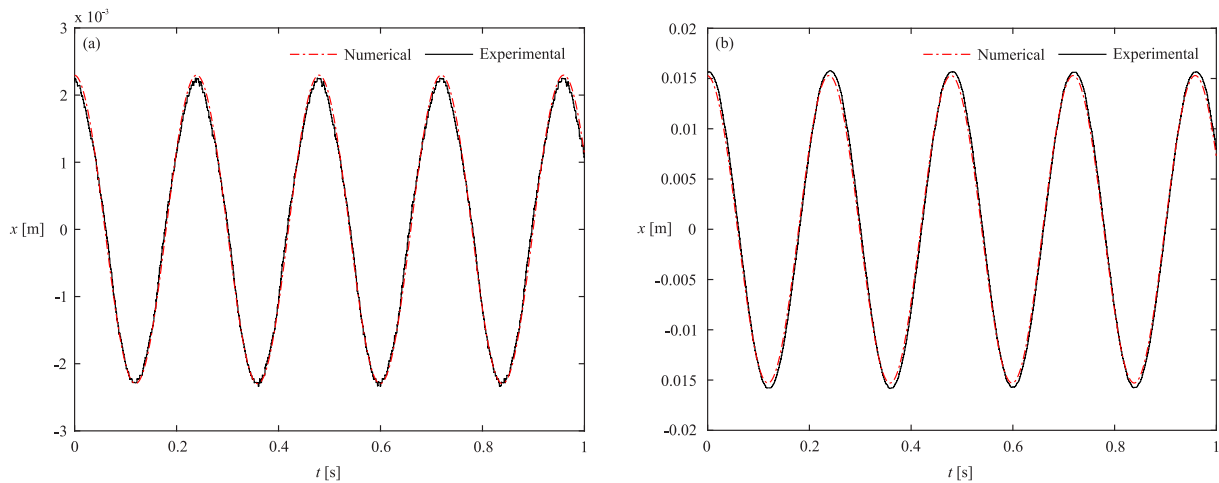


Figure 10: Comparison between numerical and experimental time traces of forced system for  $s = 250$  [rpm] and two values of inertia  $I_1 = 6.36$  (a) and  $I_2 = 12.9$  (b).

torque of internal motion resistance depends on the actual gear ratio. This important feature should be taken into consideration when designing machines including belt-driven CVTs.

Summarizing, in this paper we describe the details of the prototype TMD focusing on its crucial mechanisms. We propose simplified energy dissipation model that is crucial for the efficiency of the TMD. After the parameter identification procedure we obtain the mathematical model and validate it by comparing the experimental data with numerical simulations. We consider both free vibrations and harmonic excitation. The presented results prove the robustness of the model. The obtained results prove that the proposed TMD layout can be realized and efficiently damp out the vibrations of structures or machines in a particularly wide range of excitation frequencies.

## Acknowledgment

This work is funded by the Polish Ministry of Science and Higher Education, Iuventus Plus programme, Project No. 0352/IP2/2015/73. PB is supported by the Foundation for Polish Science (FNP) under the framework of “Start” fellowship.

## References

- [1] S. Adhikari. Structural dynamic analysis with generalized damping models: identification. *John Wiley and Sons*, 2013.
- [2] F. Bottiglione, S. De Pint and, G. Mantriota. Infinitely Variable Transmissions in neutral gear: Torque ratio and power re-circulation. *Mechanism and Machine Theory*, 74(4), 285–298, 2014.
- [3] P. Brzeski, T. Kapitaniak, and P. Perlikowski. Novel type of tuned mass damper with inerter which enables changes of inertia. *Journal of Sound and Vibration*, 349, 56–66, 2015.
- [4] P. Brzeski, M. Lazarek, and P. Perlikowski. Experimental study of the novel tuned mass damper with inerter which enables changes of inertia. *Journal of Sound and Vibration*, 404, 47–57 2017.
- [5] P. Brzeski and P. Perlikowski. Effects of play and inerter nonlinearities on the performance of tuned mass damper. *Nonlinear Dynamics*, 88, 1027–1041, 2017.
- [6] P. Brzeski, P. Perlikowski, and T. Kapitaniak. Urządzenie do tłumienia drgan, 2014.
- [7] M. Cammalleri and D. Rotella. Functional design of power-split CVTs: An uncoupled hierarchical optimized model. *Mechanism and Machine Theory*, 116: 294-309, 2017.
- [8] M.Z.Q. Chen, Y. Hu, L. Huang, and G. Chen. Influence of inerter on natural frequencies of vibration systems. *Journal of Sound and Vibration*, 333(7), 1874–1887, 2013.
- [9] Y.-C. Chen, J.-Y. Tu, and F.-C. Wang. Earthquake vibration control for buildings with inerter networks. In *Control Conference (ECC), 2015 European*, 3137–3142, July 2015.
- [10] R. Faraj, J. Holnicki-Szulc, L. Knap, and J. Senko. Adaptive inertial shock-absorber. *Smart Materials and Structures*, 25(3), 035031, 2016.

- [11] B.F. Feeny and J.W. Liang. A decrement method for the simultaneous estimation of coulomb and viscous friction. *Journal of Sound and Vibration*, 195(1), 149–154, 1996.
- [12] N.E. Houghton C. Papageorgiou and M.C. Smith. Experimental testing and analysis of inerter devices. *Journal of Dynamic Systems, Measurement, and Control*, 131, 011001–11, 2009.
- [13] J.W. Liang. Identifying coulomb and viscous damping from free-vibration acceleration decrements. *Journal of Sound and Vibration*, 282(3), 1208–1220, 2005.
- [14] J.W. Liang and B.F. Feeny. Balancing energy to estimate damping parameters in forced oscillators. *Journal of Sound and Vibration*, 295(3), 988–998, 2006.
- [15] L. Ljung. *System identification*. Wiley Online Library, 1999.
- [16] L. Ljung. Prediction error estimation methods. *Circuits, Systems and Signal Processing*, 21(1), 11–21, 2002.
- [17] P. Mall, A. Fidlín, A. Kruger and H. Gross. Simulation based optimization of torsional vibration dampers in automotive powertrains. *Mechanism and Machine Theory*, 115, 244–266, 2017.
- [18] D.C. Miller Continuously variable transmission. *US Patent US 6551210 B2*, 2003.
- [19] O. Nelles. *Nonlinear system identification: from classical approaches to neural networks and fuzzy models*. Springer Science & Business Media, 2013.
- [20] N.D. Oliveto, G. Scalia, and G. Oliveto. Dynamic identification of structural systems with viscous and friction damping. *Journal of Sound and Vibration*, 318(4), 911–926, 2008.
- [21] R.K. Pearson and M. Pottmann. Gray-box identification of block-oriented nonlinear models. *Journal of Process Control*, 10(4), 301–315, 2000.
- [22] M. Prandina, J.E. Mottershead and E. Bonisoli. An assessment of damping identification methods. *Journal of Sound and Vibration*, 323(3), 662–676, 2009.
- [23] D. Rockwood, N. Parks and D. Garmire. A continuously variable transmission for efficient urban transportation. *Sustainable Materials and Technologies*, 1, 36–41, 2014.
- [24] S.M. Savaresi, S. Bittanti, and M. Montiglio. Identification of semi-physical and black-box non-linear models: the case of mr-dampers for vehicles control. *Automatica*, 41(1), 113–127, 2005.
- [25] Ch. Shi, R. G. Parker and S. W. Shaw. Tuning of centrifugal pendulum vibration absorbers for translational and rotational vibration reduction. *Mechanism and Machine Theory*, 66, 56–65, 2013.
- [26] J. Sjöberg, Q. Zhang, L. Ljung, A. Benveniste, B. Delyon, P.-Y. Glorennec, H. Hjalmarsson, and A. Juditsky. Nonlinear black-box modeling in system identification: a unified overview. *Automatica*, 31(12), 1691–1724, 1995.
- [27] M.C. Smith. Synthesis of mechanical networks: the inerter. *Automatic Control, IEEE Transactions on*, 47(10), 1648–1662, 2002.
- [28] M.C. Smith and S.J. Swift. Design of passive vehicle suspensions for maximal least damping ratio. *Vehicle System Dynamics*, 54(5), 568–584, 2016.
- [29] N. Srivastava and I. Haque. A review on belt and chain continuously variable transmissions (CVT): Dynamics and control. *Mechanism and Machine Theory*, 44(1), 19–41, 2009.
- [30] S.J. Swift, M.C. Malcolm, A.R. Glover, Ch. Papageorgiou, B. Gartner, and H.E. Neil. Design and modelling of a fluid inerter. *International Journal of Control*, 86(11), 2035–2051, 2013.
- [31] I. Takewaki, S. Murakami, S. Yoshitomi, and M. Tsuji. Fundamental mechanism of earthquake response reduction in building structures with inertial dampers. *Structural Control and Health Monitoring*, 19(6), 590–608, 2012.
- [32] J. Wurm, M. Fitl, M. Gumpesberger, E. Vaisanen and Ch. Hochenauer. Advanced heat transfer analysis of continuously variable transmissions (CVT). *Applied Thermal Engineering*, 114, 545–553, 2017.

Appendix

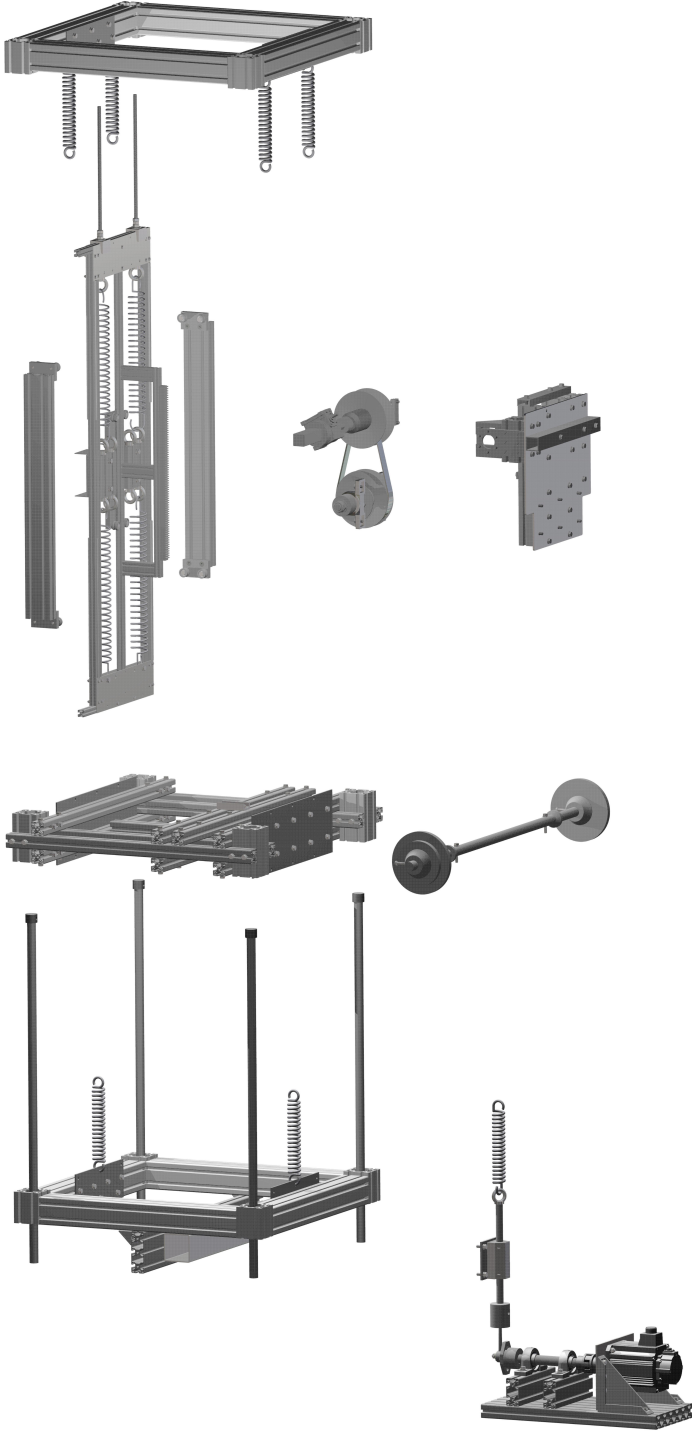


Figure 11: Exploded view of the laboratory rig. The outer steel structure is excluded from the view.